Nanoscale

Accepted Manuscript

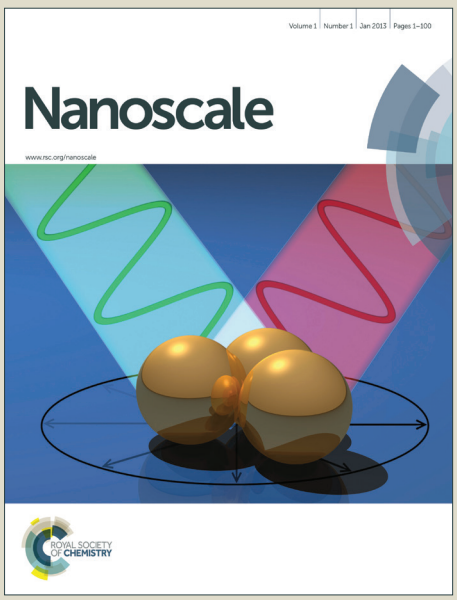

ROYAL SOCIETY OF CHEMISTRY

www.rsc.org/nanoscale

Nanoscale

ARTICLE

Ultrafast switching of electrochromic device based on layered double hydroxide/Prussian blue multilayer films

Received XXth XX 2015,
Accepted XXth XX 2015

DOI: 10.1039/x0xx00000x

www.rsc.org/

Xiaoxi Liu, Awu Zhou, Yibo Dou, Ting Pan, Mingfei Shao, Jingbin Han* and Min Wei

Electrochromic materials are the most important and essential components in an electrochromic device. Herein, we fabricated high-performance electrochromic films based on exfoliated layered double hydroxide (LDH) nanosheets and Prussian blue (PB) nanoparticles *via* layer-by-layer assembly technique. X-ray diffraction and UV-vis absorption spectroscopy indicate a periodic layered structure with uniform and regular growth of the $(LDH/PB)_n$ ultrathin films (UTFs). The resulting $(LDH/PB)_n$ UTFs electrodes exhibit electrochromic behavior arising from the reversible K^+ ion migration into/out of the PB lattice, which induces optical property change of the UTFs. Furthermore, an electrochromic device (ECD) based on $(LDH/PB)_n$-ITO/0.1 M KCl electrolyte/ITO sandwich structure displays superior response property (0.91/1.21 s for coloration/bleaching), comparable coloration efficiency (68 cm^2/C) and satisfactory optical contrast (45% at 700 nm), in comparison with other inorganic materials-based ECDs reported previously. Therefore, this work presents a facile and cost-effective strategy to immobilize electrochemical active nanoparticles in 2D inorganic matrix for the potential application in displays, smart windows and optoelectronic devices.

1.Introduction

Electrochromic (EC) materials can reversibly change their optical properties under applied voltage as a result of the electrochemical redox reaction, which enables them as good candidates for extensive applications, including displays, antiglare rear-view mirrors, smart windows and military camouflage.[1-3] It has been approved that the inorganic EC materials, e.g., WO_3, Nb_2O_5, MoO_3, NiO and TiO_2, exhibit coloration (or decoloration) under applied voltage due to the intercalation of small ions into their lattices.[4-6] The intercalation leads to additional electronic states in the band gap of the EC materials, which in turn affects the change in their optical properties. When an opposite voltage is applied, the small ions are extracted out of the material lattices, which results in decoloration (or coloration). In comparison with organic counterparts, inorganic EC materials possess the advantages of excellent electrochemical stability, environmental friendliness and low cost. However, the response time of inorganic EC materials is relatively long (up to tens of seconds), owing to high diffusion resistance of electrolyte ions arising from disordered stacking or serious aggregation of inorganic particles, which limits their practical application in optical devices and sensors. To overcome this limitation, inorganic EC materials have been tailored into nanostructures to increase available surface area and shorten ion diffusion length, such as nanoporous NiO,[5] TiO_2-WO_3 composite nanotubes,[7] WO_x-carbon nanotube[8] and WO_3 nanocrystal.[9, 10] Although extensive efforts have been dedicated to the improvement of response property of inorganic EC materials, the slow response rate still can not satisfy the high requirements of electrochromic devices.[11-15] Therefore, it is highly essential to explore new methodologies to fabricate novel materials with enhanced ions diffusion and subsequently to improve the electrochromic performance.

Prussian blue (PB), $KFe^{III}[Fe^{II}(CN)_6]$ is known as an important functional transition metal hexacyanoferrate,[16-18] in term of its electrochemical, electrochromic and magnetic properties.[19-24] The suitable redox reaction region and excellent electrochromic properties make it a prominent candidate for electrochromic displays.[25, 26] To date, several fabrication techniques have been applied for the assembly or incorporation of PB into the desired nanostructures to achieve electronic and electrochemical devices.[27-29] However, the aggregation of PB nanoparticles (NPs) is normally inevitable due to their high surface energy, which leads to the low utilization of PB NPs active sites and the long response time, which finally result in mediocre electrochromic performance.[30, 31] Therefore, the construction of suitable hybrid structure with good dispersity of PB NPs and facile ion channel for fast electrolyte diffusion would be a feasible strategy to solve this issue.

Layered double hydroxides (LDHs), whose formula can be generally expressed as $[M^{2+}_{1-x}M^{3+}_x(OH)_2]^{x+}[A^{n-}_{x/n}]^{x-} \cdot mH_2O$ (M^{2+} and M^{3+} represent di- and tri-valent metal cations, respectively; A^{n-} is a *n*-valent anion), are a class of two dimensional (2D) layered materials.[32-34] By virtue of the specific layered structure, intercalation property, non-toxicity and biocompatibility, LDH materials have been used in the fields of catalysis, biology, optical devices and electrochemical sensors.[35-37] Recently, LDHs have been exfoliated into positively charged nanosheets with a theoretical thickness of 0.48 nm,[38] which are considered as one of the most promising building blocks[39, 40] for the fabrication of electrochemical devices due to their permeable ion channels and high accessible surface areas.[41] In this regard, the incorporation of LDHs nanosheets with PB NPs into an ordered film with good dispersity would be a preferable resolution for the enhancement of electrochemical performances.

State Key Laboratory of Chemical Resource Engineering, Beijing University of Chemical Technology, Beijing, 100029, China. *E-mail: hanjb@mail.buct.edu.cn. Fax: +86-10-64425385; Tel: +86-10-64412131*

† Electronic Supplementary Information (ESI) available. See DOI: 10.1039/x0xx00000x

In this work, negatively charged PB NPs were assembled alternately with positively charged LDH nanosheets on ITO substrate *via* the electrostatic layer-by-layer (LBL) deposition technique. The $(LDH/PB)_n$ films display an excellent EC behavior with fast switching speed and high optical contrast under different applied voltage (Scheme 1). In addition, a EC device was further fabricated using $(LDH/PB)_n$ ultrathin film as working electrode, which manifested a low response time, long-term stability and good memory effect, realizing one step closer for practical applications.

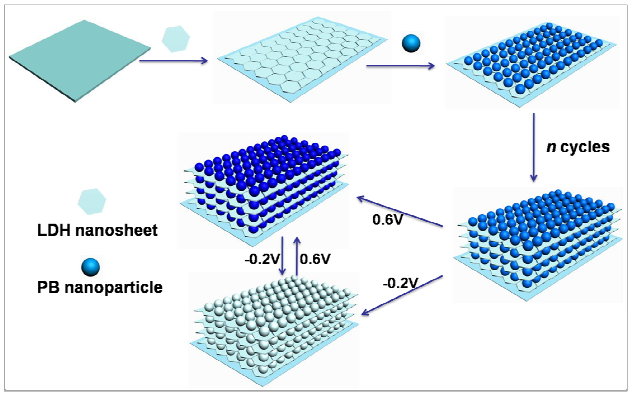

Scheme 1. Schematic representation for the LBL fabrication of multilayer $(LDH/PB)_n$ electrochromic film.

2. Experimental section

2.1 Preparation of PB NPs and MgAl-LDH nanosheets

PB NPs suspension was synthesized according to the previous report.[16] The aqueous solution of $FeCl_2$ (35 mL, 0.01 M) was added dropwise to a mixed solution (35 mL) containing potassium ferricyanide (0.05 M) and KCl (0.05 M), and then the solution was vigorously agitated for 10 min under room temperature. Afterwards, the resulting solution was dialysed for 48 h to remove the excess ions. After adjustment of the pH value (by using dilute hydrochloric acid) to 5, a very stable blue colloidal solution was obtained.

The process for synthesis and exfoliation of MgAl-LDH was similar to the procedure described in our previous work.[42-44] The $MgAl(CO_3)$-LDH platelets with narrow size-distribution and high crystallinity were prepared by a homogeneous coprecipitation method. Typically, the mixed solution (100 mL) containing $Mg(NO_3)_2{\cdot}6H_2O$ (0.2 M), $Al(NO_3)_3{\cdot}9H_2O$ (0.1 M) and urea (1 M) was vigorously agitated; and then it was transferred into an autoclave at 110□ for 24 h. The precipitate was centrifuged and washed three times with deionized water and dried in air at 60□. The $MgAl(NO_3)$-LDH platelets were prepared by a so-called salt-acid method: $MgAl(CO_3)$-LDH platelets (1.0 g) were treated with aqueous salt-acid solution (1 L) containing HNO_3 (0.0045 mol) and $NaNO_3$ (1.5 mol) in a flask under nitrogen flow and continuous stirring under room temperature for 24 h. The resulting $MgAl(NO_3)$-LDH platelets were centrifuged, washed and dried. Subsequently, 0.1 g of $MgAl(NO_3)$-LDH platelets were dispersed in 100 mL formamide for 48 h to produce a colloidal suspension of single-layer MgAl-LDH nanosheets.

2.2 Fabrication of the $(LDH/PB)_n$ multilayer films

The $(LDH/PB)_n$ films were fabricated by LBL deposition method. Prior to assembly, the ITO glass substrates were ultrasonic cleaned by immersion into deionized water, ethyl alcohol for 10 min in sequence. The treated substrates were dipped into a colloidal suspension of LDH nanosheets (1 g/L) for 10 min followed by washing thoroughly. After that, the substrates were immersed into PB NPs colloidal suspension (3.5 g/L) for another 10 min and washed. Multilayer films of $(LDH/PB)_n$ were prepared by alternate deposition of LDH nanosheets and PB NPs colloidal suspension for *n* cycles. For a comparison study, $(PDDA/PB)_n$ film was fabricated *via* a similar LBL procedure; and pure PB film was obtained by a spin-coating technique.

2.3 Assembly of the EC device

For the electrochromic measurement, an electrochromic device based on a $(LDH/PB)_n$-ITO/0.1 M KCl electrolyte/ITO glass sandwich structure was prepared by three steps. In the first step, the as-prepared $(LDH/PB)_n$-ITO electrode and counter ITO glass were attached by Surlyn hot-melt adhesive with one pore set apart. In the second step, 0.1 M KCl aqueous solution was injected with a microbore needle, through the unsealed pore by capillary action on gently squeezing until all bubbles were expelled. Finally, the hole was sealed with a hot-melt sealer. Thus, the sandwich-type electrochromic device was assembled successfully.

2.4 Characterization

The particle size and morphology of PB NPs were characterized by JEOL JEM-2010 high-resolution transmission electron microscopy (HRTEM). The morphologies of thin films were investigated by using a scanning electron microscope (SEM, Hitachi S-3500) equipped with an EDX attachment (EDX Oxford Instrument Isis 300), and the accelerating voltage applied was 20 kV. Zeta potential measurement was performed on Zetasizer Nano ZS (Malvern) using a clear zeta cell for a minimum of 12 runs. The surface roughness data was obtained by using the NanoScope IIIa atomic force microscope (AFM) from Veeco Instruments. The interlayer spacing of the prepared film was tested by X-ray diffraction patterns (XRD) using a Rigaku 2500 VB2+PC diffractometer under the conditions: 40 kV, 50 mA, Cu K radiation (λ=0.1542 nm). The UV-vis absorption spectra were collected in the range 320–800 nm on a Shimadzu U-3000 spectrophotometer, with the slit width of 1.0 nm. Cyclic voltammograms were measured by CHI660B electrochemical workstation in a conventional three-electrode cell in 0.1 M KCl aqueous solution within the potential window of –0.2 to 0.6 V. Electrochemical impedance spectra (EIS) measurements were performed by applying an alternating current voltage with 5 mV amplitude in a frequency range from 0.01 to 100 kHz. X-ray photoelectron spectra (XPS) were recorded on a Thermo VG Escalab 250 X-ray photoelectron spectrometer at a pressure of about 2×10^{-9} Pa with Al 193 Kα X-rays as the excitation source. The Fouriertransform infrared (FT-IR) spectra were obtained using a Vector 22 (Bruker) spectrophotometer with 2 cm^{-1} resolution. The coloration/bleaching switching characteristics of the electrochromic device were measured by transmittance variation at a wavelength of 700 nm with alternately applying potential of –1 and 1 V, keeping for 5 s in each state.

3. Results and discussion

3.1 Characterization of LDH nanosheets and PB NPs

The XRD pattern (black line in Fig S1, ESI†) of the synthesized MgAl(CO_3)-LDH displays a series of reflections at 11.7°, 23.5°, 34.8°, 59.7° and 60.9°, corresponding to the (003), (006), (012), (110) and (113) reflections of LDH phase. No other crystalline phase is detected, indicating a well-defined CO_3^{2-} containing LDH with high crystallinity. Then the MgAl(NO_3)-LDH was prepared through ion exchange of interlayer CO_3^{2-} by NO_3^- ion under N_2 shielding. An obvious peak shift of the (00*l*) planes (red line in Fig. S1, ESI†) was observed, corresponding to the successful preparation of the MgAl(NO_3)-LDH. The transmission electron microscopy (TEM) image (Fig. 1a) reveals a hexagonal plate-like morphology of MgAl(NO_3)-LDH with particle size of 4–8 μm. The MgAl-LDH nanosheets were prepared by exfoliating the MgAl(NO_3)-LDH platelet in formamide. Atomic force microscope (AFM) image shows the sheet-like morphology with a thickness of ~0.8 nm (inset Fig. 1b), indicating a complete delamination of MgAl(NO_3)-LDH platelet into single-layer nanosheets, which provides ideal building blocks for the fabrication of multilayer films.

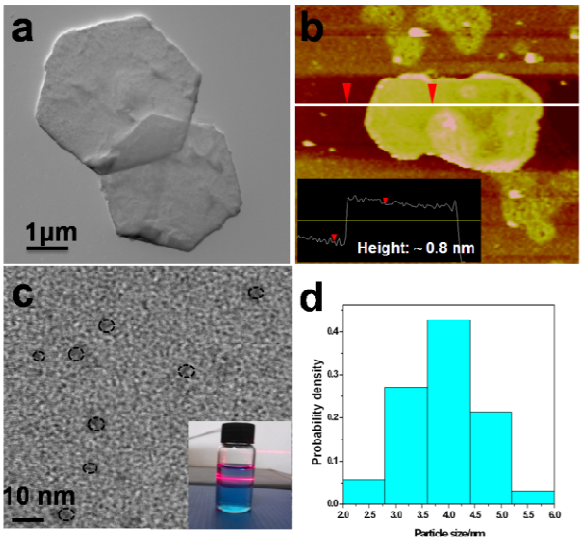

Fig. 1 a) TEM image of the MgAl(NO_3)-LDH platelet; b) AFM image of the exfoliated LDH nanosheets; c) TEM image of the PB NPs (inset: the PB colloidal dispersion displaying the Tyndall effect); d) the corresponding size distribution of PB NPs.

The particle size of PB NPs was determined using high-resolution transmission electron microscopy (HRTEM, Fig. 1c), which demonstrates a uniform size distribution from 3 nm to 5 nm with a mean size of 3.77 nm (Fig. 1d). A clear Tyndall light scattering effect was observed for the dark blue PB NPs suspension by a side-incident light beam (inset of Fig. 1c); and the well-dispersed PB NPs can be stored for more than two months, reasonably inferring the formation of stable and homogeneous colloidal suspension. The UV-vis spectrum of PB NPs colloidal suspension displays a strong maximum absorbance around 700 nm (Fig. S2, ESI†), which is attributed to the absorption of mixed-valence compound and the photo-induced electron transfer from Fe^{II} to Fe^{III}.[26, 30]

3.2 Structural and morphological characterization of the $(LDH/PB)_n$ ultrathin films (UTFs)

The surface charge character of LDH nanosheets and PB NPs was investigated by zeta potential measurement (Fig. S3, ESI†), which reveals positively- and negatively-charged surface for LDH nanosheets (+20.0 mV) and PB NPs (−16.6 mV), respectively. The $(LDH/PB)_n$ UTFs were fabricated by alternate assembly of MgAl-LDH nanosheets with PB NPs on ITO-glass substrate. The fabrication process of $(LDH/PB)_n$ UTFs was monitored by UV-vis absorption spectroscopy as depicted in Fig. 2a. The $(LDH/PB)_n$ UTFs exhibit a strong absorption band at ~700 nm and there is no obviously shift in comparison with the PB colloidal suspension, which indicates the good dispersity of PB NPs in the $(LDH/PB)_n$ UTFs. The inset in Fig. 2 shows a linear growth of the band intensity at 700 nm with increasing the bilayer number *n*, indicating a stepwise and regular film deposition procedure. The small angle XRD patterns of the $(LDH/PB)_n$ UTFs (Fig. 2b) display a reflection at about 2θ=2.04° with a periodic repeating distance of 4.41 nm, which refers to monolayer arrangement of PB NPs in the $(LDH/PB)_n$ films. The enhanced intensity of the reflection upon increasing the deposition cycle indicates a periodic ordered superlattice structure of these UTFs. The alternate assembly of LDH nanosheets and PB NPs was further confirmed by TEM. As shown in Fig. S4 (ESI†), a lattice fringes with a spacing of ~4 nm was observed, indicating a high-quality superlattice arrangement of the $(LDH/PB)_n$ films.

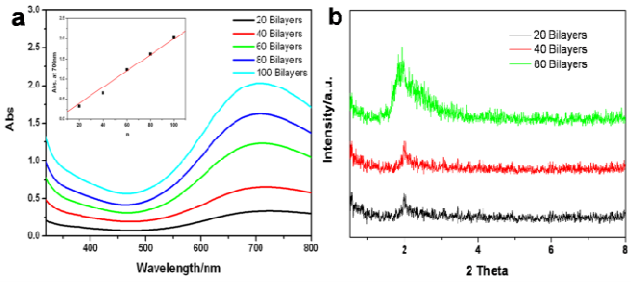

Fig. 2 a) UV-vis spectra of the $(LDH/PB)_n$ (*n*=20, 40, 60, 80 and 100) UTFs (inset: the linear relationship between the absorbance at 700 nm and bilayer number *n*); b) XRD patterns of the $(LDH/PB)_n$ UTFs (*n*=20, 40 and 80).

The surface morphology, thickness and roughness of the $(LDH/PB)_n$ UTFs were studied by SEM and AFM. Highly homogeneous and continuous surfaces were clearly observed in the SEM images of the $(LDH/PB)_n$ UTFs (Fig. S5, a1~a5, ESI†). The cross-sectional SEM images (inset in Fig. S5, a1~a5, ESI†) display an uniform layered architecture with a thickness of ~4 nm for one bilayer of LDH/PB in the UTFs, which is consistent with the XRD and TEM results. The AFM topographical images of the $(LDH/PB)_n$ films (Fig. S5, b1~b5, ESI†) indicate a root-mean-square roughness of 4.43, 6.32, 7.91, 9.32 and 12.95 nm for the $(LDH/PB)_n$ UTFs with *n*=20, 40, 60, 80 and 100, respectively, illustrating the continuous and smooth surface of these films.

3.3 Electrochemical and electrochromic properties of the $(LDH/PB)_n$ UTFs

The electrochemical behavior of $(LDH/PB)_n$ films were characterized by cyclic voltammetry (CV) in a three-electrode system in 0.1 M KCl aqueous electrolyte. The CV curves of $(LDH/PB)_n$ UTFs modified ITO electrodes with different bilayer

numbers (Fig. 3a) show a pair of redox peaks, corresponding to the transformation between oxidized $KFe^{III}[Fe^{II}(CN)_6]$ (PB) and reduced $K_2Fe^{II}[Fe^{II}(CN)_6]$ (Prussian white, PW). The redox current presents consistent enhancement with the increase of bilayer number *n*, also demonstrating an ordered and regular film growth procedure. In addition, the oxidative and reductive potentials of $(LDH/PB)_n$ UTFs show a tiny shift upon increasing film thickness, which is smaller than most of the other PB-based film electrodes,[16] indicating a relatively low ion-diffusion resistance of the $(LDH/PB)_n$ films.

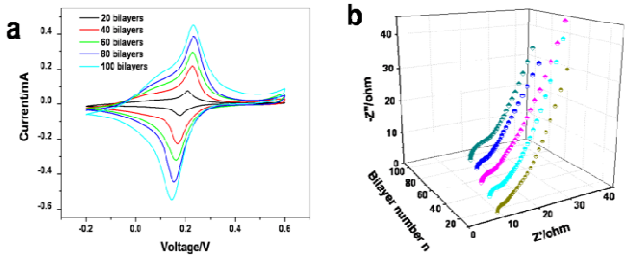

Fig. 3 a) Cyclic voltammograms (scan rate: 20 mV/s); b) Nyquist plots of the $(LDH/PB)_n$ films (n=20–100).

To further illustrate the electrochemical reaction between PB and PW, XPS measurements for $(LDH/PB)_n$ film at different voltages as well as two reference compounds ($K_4[Fe^{II}(CN)_6]$ and $K_3[Fe^{III}(CN)_6]$) were carried out (Fig S6, ESI†). At bias of 0.6 V, two peaks located at 708.5 and 711.2 eV are observed, corresponding to the Fe^{II} and Fe^{III} in oxidized $KFe^{III}[Fe^{II}(CN)_6]$, respectively. After reducing at an applied potential of –0.2 V, the peak at 711.2 eV disappears, corresponding to the formation of PW, $K_2Fe^{II}[Fe^{II}(CN)_6]$. Furthermore, at a bias of 0.6 V, the FT-IR spectrum of PB (Fig. S7, ESI†) exhibits stretching vibration of CN group at 2083 cm^{-1} as well as Fe^{II}–CN–Fe^{III} vibration at 498 cm^{-1}.[45, 46] After the alteration of applied voltage to –0.2 V, the stretching vibration of CN group shifts to a lower wave number and the Fe^{II}–CN–Fe^{III} vibration disappears, indicating the absence of Fe^{III} in the PW state.

Electrochemical impedance spectroscopy (EIS) was applied in order to study the ion diffusion and electron transfer property of the obtained $(LDH/PB)_n$ films (Fig. 3b). The $(LDH/PB)_n$ electrodes with different bilayer number all display similar plots with a semicircle at high frequency region and a straight line at low frequency. The equivalent series resistance (ESR) rises with the increase of film thickness, which demonstrates an increased resistance in the electrode-electrolyte interface. The linear part in the low frequency region corresponds to the Warburg impedance (W), which is described as a diffusive resistance of the K^+ ion within the electrode pores. As shown in the EIS curves, the slopes of the five straight lines are far greater than 1, with no significant change for various bilayer numbers. This result indicates that the electrolyte diffusion resistance for the $(LDH/PB)_n$ films electrodes is relatively low, which is in favour of their electrochemical reaction dynamics.

The electrochromic behavior of the $(LDH/PB)_{60}$ film was studied in a three electrodes system by linear sweep voltammetry and UV-vis absorption spectroscopy. Fig. 4a shows the transmittance spectra and the corresponding transmittance spectra and the corresponding photographs the corresponding photographs of $(LDH/PB)_{60}$ electrode under applied potentials of –0.2 V and 0.6 V, respectively. From the transmittance spectra, it can be seen that the optical transmittance is 20% in the colored state (0.6 V) and 76%

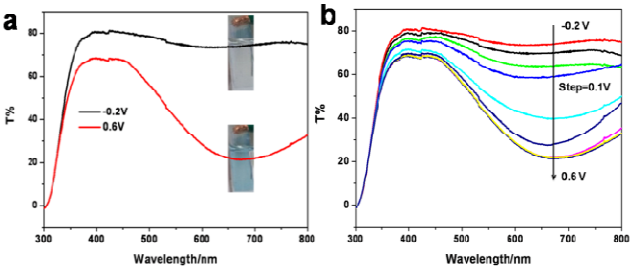

Fig. 4 a) Optical transmittance spectra of the $(LDH/PB)_{60}$ film at the colored and bleached states (the photographs of the film at colored and bleached states); b) spectroelectrochemical study of the $(LDH/PB)_{60}$ film from –0.2 to 0.6 V with a stepwise of 0.1 V.

in the bleached state (–0.2 V) at 700 nm, indicating a noticeable electrochromism with variation of transmittance to 56%. The inset image of Fig. 4a shows the color change of $(LDH/PB)_{60}$ film between colorless and blue. In Fig. 4b, we present the optical transmittance of the $(LDH/PB)_{60}$ film electrode in different voltage from –0.2 V to 0.6 V with a voltage step of 0.1 V. As the electrode potential becomes more anodic from –0.2 V, the optical transmittance decreases gradually, corresponding to the electrochemical reaction from PW to PB in the electrode. Meanwhile, the transmittance contrast varies from 19.2% to 69.8% as *n* increases from 20 to 100, which does not undergo obvious change with further increase of bilayer number (Fig. S8, ESI†).

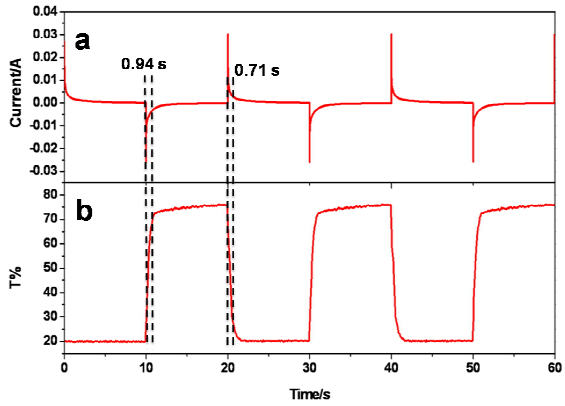

Fig. 5 a) Chronoamperometry curve and b) corresponding *in situ* optical transmittance change at 700 nm for the $(LDH/PB)_{60}$ film under switched voltage between 0.6 and –0.2 V.

The color-switching time of $(LDH/PB)_n$ films was obtained by recording chronoamperometry curve and *in situ* transmittance at 700 nm through alternate bias at 0.6 and –0.2 V (Fig. 5). The response time is defined as the time to reach 90% of its full modulation. The color-switching time of $(LDH/PB)_{60}$ film is 0.71 s from bleached state to colored state and 0.94 s for the reverse process with a optical contrast (ΔT%) of 56.0%. The switching time and optical contrast of $(LDH/PB)_n$ films with different bilayer number are summarized in Table 1. As *n* increases from 20 to 80, the coloring/bleaching time gradually increases from 0.15/0.19 to 0.93/1.21 s, respectively. A

further increase of bilayer number results in a sharp increase of response time, which is likely attributed to the largely depressed ion transfer in thick film. For instance, the switching times of $(LDH/PB)_{100}$ film for coloration and fading are 1.32 and 1.96 s, respectively. The response time of the $(LDH/PB)_n$ films with n<80 is much lower than most of inorganic electrochromic films, including PB NPs/graphene hybrids,[12] TiO_2 nanotube arrays/WO_3 NPs,[4] and nanostructured NiO.[47] Such ultrafast switching is favorable to various applications, including sensors, smart widows or other electrochromic devices.

There are two types of redox reactions that occur in an electrochromic process: charge transfer at the materials-electrolyte interface and diffusion controlled redox reaction within the material lattices. Since the rate-determining steps of ion intercalation and deintercalation is diffusion-controlled and limited to a very thin surface layer of the materials. Thus the response time of reversible transition between PW and PB is controlled by the diffusion rate of K^+ intercalation/deintercalation process. To evaluate the K^+ diffusioncoefficient in the $(LDH/PB)_n$ films, the CV curves of these films on ITO electrodes were carried out with different scan rates (Fig. 6a). The relationship between the peak currents (i_p) and scan rate (v) was evaluated by a series plots of i_p versus v^x with x = 0.5–1. By plotting the peak current value versus the square root of the scan speed, straight lines are obtained (Fig. 6b), which suggests that the K^+ insertion and extraction are very fast and the rate-determining step is controlled by diffusion of K^+ in these films. The K^+ diffusion coefficient can be calculated from a linear relationship between i_p and $v^{1/2}$ according to the following equation:

$$i_p = 2.69\times10^5 n^{2/3} A D^{1/2} C v^{1/2}$$

where i_p is the peak current (A); A is the electrode area (cm^2); D is the apparent diffusion coefficient of K^+ in the electrode ($cm^2\ s^{-1}$); C is the concentration of K^+ in the electrode (mol cm^{-3}), and v is the potential scan rate (V s^{-1}).

Table 1. Switching time and optical contrast of the $(LDH/PB)_n$ films with various bilayer number n

Bilayer (n)	Coloring time/s	Bleaching time/s	ΔT% (λ=700 nm)
20	0.15	0.19	19.2
40	0.42	0.48	27.6
60	0.71	0.94	56.0
80	0.93	1.21	64.3
100	1.32	1.96	69.8

To further illustrate the effects of ordered structure and high dispersion of PB on the diffusion rate of K^+ in the $(LDH/PB)_n$ electrodes, disordered $(PDDA/PB)_n$ film and aggregated pure PB film were prepared by LBL and spin-coating technique, respectively, for a comparison study. The amount of active component PB NPs in each sample was controlled at the same level. CV curves of these films on ITO substrates were carried out to find the same integral area as the referential samples. As shown in Fig. S9 (ESI†), the $(LDH/PB)_{20}$, $(PDDA/PB)_{60}$ and PB were chosen as the final samples. According to the above equation, the diffusion coefficients of K^+ in the $(LDH/PB)_{20}$, $(PDDA/PB)_{60}$ and pure PB films were calculated and summarized in Table 2.

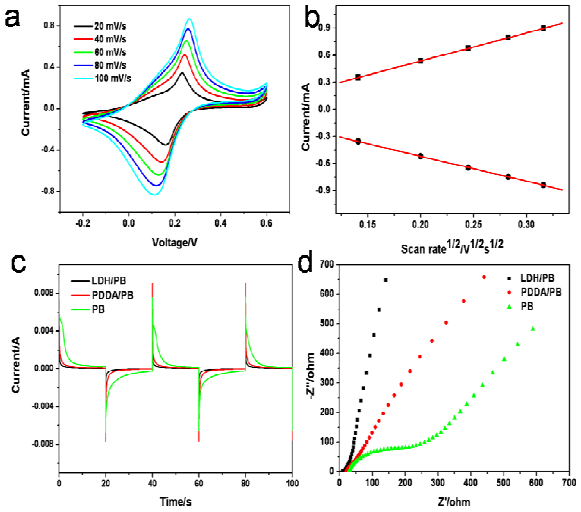

Fig. 6 a) CV curves of the $(LDH/PB)_{60}$ film at different scan rates; b) the cathodic/anodic peak current as a function of the square root of scan rate for the $(LDH/PB)_{60}$ film; c) the response time and d) Nyquist plots for the $(LDH/PB)_{20}$, $(PDDA/PB)_{60}$ and pure PB films.

For the $(LDH/PB)_{20}$ film, the calculated K^+ diffusion coefficients are 1.33×10^{-8} and 1.06×10^{-8} $cm^2\ s^{-1}$ for the intercalation and deintercalation process, respectively. As is expected, the K^+ diffusion coefficients of $(LDH/PB)_{20}$ film are much larger than those of $(PDDA/PB)_{60}$ film (7.89×10^{-10} and 1.13×10^{-9} $cm^2\ s^{-1}$) and pure PB film (5.70×10^{-10} and 8.91×10^{-10} $cm^2\ s^{-1}$). In addition, the $(LDH/PB)_{20}$ film exhibits faster coloration/bleaching switching with 0.15/0.19 s, in comparison to $(PDDA/PB)_{60}$ (0.31/0.37 s) and PB films (4.2/4.8 s) (Fig. 6c). The larger K^+ diffusion coefficient and shorter switching time of $(LDH/PB)_{20}$ film are attributed to the ordered structure and high dispersion of PB NPs, which results in reduced ion diffusion resistance between the active component and electrolyte.

Table 2. K^+ diffusion coefficient in the $(LDH/PB)_{20}$, $(PDDA/PB)_{60}$ and pure PB films

Sample	Intercalation	Deintercalation
$(LDH/PB)_{20}$	1.33×10^{-8}	1.06×10^{-8}
$(PDDA/PB)_{60}$	7.89×10^{-10}	1.13×10^{-10}
PB	5.70×10^{-10}	8.91×10^{-10}

The diffusion of K^+ ion was also illustrated by the EIS study, which provides information about the K^+ diffusion resistance within the electrode pores. As shown in Fig. 6d, the slope of the straight line for well-oriented $(LDH/PB)_{20}$ film is larger than that of randomly stacked $(PDDA/PB)_{60}$ and PB films, indicating the superior diffusion dynamics of $(LDH/PB)_{20}$ electrode. Moreover, the $(LDH/PB)_{20}$ film with a smaller diameter in a higher frequency region is observed, which illustrates its higher electron transport rate and lower interface resistance. This result is in consistent with the faster color-switching rate of $(LDH/PB)_{20}$ electrode by opticalelectrochemical measurements.

3.4 Electrochemic properties of the electrochromic device

In order to demonstrate the potential of the $(LDH/PB)_n$ film electrodes for practical application, an electrochromic device (ECD) was assembled as shown in Fig. 7a. The ECD was prepared using a $(LDH/PB)_{60}$ film on ITO-glass electrode and a bare ITO-glass, with 0.1M KCl as electrolyte. Fig. 7b shows the transmittance spectra and the corresponding photographs of the $(LDH/PB)_{60}$-ITO/0.1 M KCl electrolyte/ITO-glass ECD for the colored and bleached states, respectively. From the transmittance spectra, it can be seen that the optical transmittance of ECD is 73.1% for the bleached state and 28.5% for the colored state at a wavelength of 700 nm, accompanied by its visual electrochromic behavior between colorless and blue.

The coloration efficiency (*CE*) is a key parameter for electrochromic devices, since a high *CE* can provide a large optical modulation with low charge insertion or extraction. It is expressed as $CE(\lambda)=\Delta A(\lambda)/\Delta Q(\lambda)$, where $\Delta Q(\lambda)$ is the corresponding accumulated charge for absorbance change $\Delta A(\lambda)$. Fig. 7c shows plot of the *in situ* optical density at a wavelength of 700 nm versus inserted charge density at a coloration potential of –1 V. A fitted linear relationship is obtained from the initial part of the plot. Based on the slope of such linear relationship, the *CE* of the $(LDH/PB)_{60}$- ITO/0.1 M KCl electrolyte/ITO-glass ECD is measured to be 68 cm^2/C. The coloration efficiency is comparable to those of the ECDs based on patterned PB/FTO,[48] polyaniline-WO_3[49] and NiO nanoparticle films[50] but lower than the nanoporous WO_3[51] and Nb_2O_5[52] ECDs.

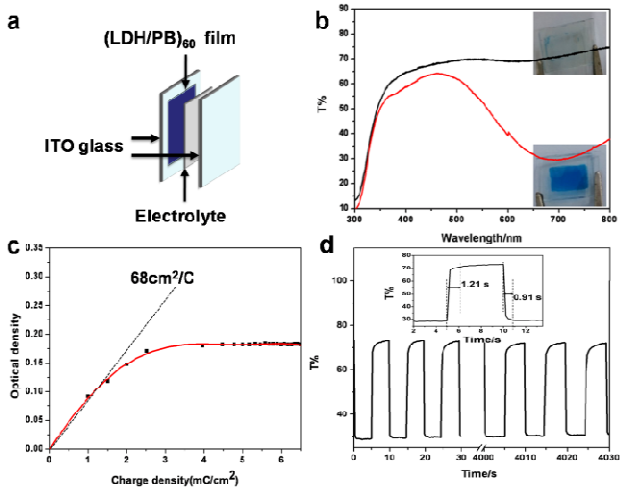

Fig. 7 a) Schematic of the $(LDH/PB)_{60}$-ITO/0.1 M KCl electrolyte/ITO-glass ECD; b) optical transmittance spectra and photographs of the ECD under potentials of 1 and –1 V, respectively; c) variation of the *in situ* optical density at 700 nm *vs*. charge density of the ECD; d) optical transmittance change at 700 nm *vs*. time for the ECD during double potential steps between 1 and –1 V.

The switching time is another important factor in the practical applications, which was studied by a transmittance measurement at a alternating bias between 1 and –1 V. As shown in the inset of Fig. 7d, the switching time of this device with an active area of 1 × 1.5 cm^2 is 0.91 s from the bleached to colored state and 1.21 s for the reverse process. The response time is less than most of reported ECDs, including TiO_2/PB NPs,[20] NiO microflake,[5] WO_3 nanosheet[38] and WO_3/silver nanowire[53] based devices. Moreover, Fig. 7d shows that the ECD maintains its electrochromic property in 400 switching cycles, without obvious change in optical contrast, switching time and surface morphology (Fig. S10, ESI†), indicating its excellent cycling stability. The optical contrast undergoes slow degradation after 400 cycles, with ~50% maintenance after 1000 cycles (Fig. S11, ESI†). And the stability is superior to previously reported inorganic WO_3/silver nanowire,[53] nanostructured NiO[54] and TiO_2 nanowire[55] films. In addition, there is a negligible change in the transmittance after withdrawing the applied potential for 24 h (Fig. S12, ESI†), demonstrating a good memory effect of the ECD. Therefore, the ultrafast switching, high coloration efficiency, together with the satisfactory optical contrast and good stability, would hold promise for its prospective application as electrochromic material.

4. Conclusions

In summary, $(LDH/PB)_n$ films with significantly enhanced electrochromic property were successfully fabricated on ITO electrodes *via* LBL assembly technique. The structural and morphological studies illustrate long-range stacking order of the $(LDH/PB)_n$ films, in which PB NPs are highly dispersed and immobilized with a monolayer arrangement in the LDH interlayer. The obtained $(LDH/PB)_n$ films exhibit fast response speed, large optical contrast, high coloration efficiency and good cycling stability. These superior electrochromic performances can be ascribed to the high dispersion of PB NPs within an ordered film structure, which guarantees facile K^+ ion diffusion channels and enhanced availability of active sites. It is prospected that this versatile and cost-effective strategy can be used to immobilize other functional nanoparticles in 2D inorganic matrix for the potential applications in displays, smart windows and optoelectronic devices.

Acknowledgements

This work was supported by the 863 Program (Grant no.2013AA032501), the National Natural Science Foundation of China (NSFC), the Doctoral Fund of Ministry of Education of China (20120010120010) and the Beijing Natural Science Foundation (2132043). M. Wei particularly appreciates the financial aid from the China National Funds for Distinguished Young Scientists of the NSFC.

Notes and references

1. D. M. DeLongchamp and P. T. Hammond, *Chem. Mater.*, 2004, **16**, 4799-4805.
2. S. Araki, K. Nakamura, K. Kobayashi, A. Tsuboi and N. Kobayashi, *Adv. Mater.*, 2012, **24**, 122-126.
3. W. Weng, T. Higuchi, M. Suzuki, T. Fukuoka, T. Shimomura, M. Ono, L. Radhakrishnan, H. Wang, N. Suzuki, H. Oveisi and Y. Yamauchi, *Angew. Chem. Int. Ed.*, 2010, **49**, 3956-3959.
4. Y.-Y. Song, Z.-D. Gao, J.-H. Wang, X.-H. Xia and R. Lynch, *Adv. Funct. Mater.*, 2011, **21**, 1941-1946.
5. D. Ma, G. Shi, H. Wang, Q. Zhang and Y. Li, *Nanoscale*, 2013, **5**, 4808-4815.

6. G.-F. Cai, J.-P. Tu, J. Zhang, Y.-J. Mai, Y. Lu, C.-D. Gu and X.-L. Wang, *Nanoscale*, 2012, **4**, 5724-5730.
7. Y. C. Nah, A. Ghicov, D. Kim, S. Berger and P. Schmuki, *J. Am. Chem. Soc.*, 2008, **130**, 16154-16155.
8. Z. Yao, J. Di, Z. Yong, Z. Zhao and Q. Li, *Chem. Commun.*, 2012, **48**, 8252-8254.
9. S. H. Lee, R. Deshpande, P. A. Parilla, K. M. Jones, B. To, A. H. Mahan and A. C. Dillon, *Adv. Mater.*, 2006, **18**, 763-766.
10. P. Yang, P. Sun, Z. Chai, L. Huang, X. Cai, S. Tan, J. Song and W. Mai, *Angew. Chem. Int. Ed.*, 2014, **53**, 11935-11939.
11. J. Z. Chen, W. Y. Ko, Y. C. Yen, P. H. Chen and K. J. Lin, *ACS Nano*, 2012, **6**, 6633-6639.
12. J. H. Ko, S. Yeo, J. H. Park, J. Choi, C. Noh and S. U. Son, *Chem. Commun.*, 2012, **48**, 3884-3886.
13. J. Jensen, M. Hösel, I. Kim, J.-S. Yu, J. Jo and F. C. Krebs, *Adv. Funct. Mater.*, 2014, **24**, 1228-1233.
14. Y. S. Nam, H. Park, A. P. Magyar, D. S. Yun, T. S. Pollom and A. M. Belcher, *Nanoscale*, 2012, **4**, 3405-3409.
15. H. Zhang, G. Duan, G. Liu, Y. Li, X. Xu, Z. Dai, J. Wang and W. Cai, *Nanoscale*, 2013, **5**, 2460-2468.
16. D. M. DeLongchamp and P. T. Hammond, *Adv. Funct. Mater.*, 2004, **14**, 224-232.
17. G. Rogez, S. Parsons, C. Paulsen, V. Villar and T. Mallah, *Inorg. Chem.*, 2001, **40**, 3836-3837.
18. H. J. Buser, D. Schwarzenbach, W. Petter and A. Ludi, *Inorg. Chem.*, 1977, **16**, 2704-2710.
19. L. Han, L. Bai and S. Dong, *Chem. Commun.*, 2014, **50**, 802-804.
20. K. Szacilowski, W. Macyk and G. Y. Stochel, *J. Mater. Chem.*, 2006, **16**, 4603-4611.
21. O. Sato, T. Kawakami, M. Kimura, S. Hishiya, S. Kubo and Y. Einaga, *J. Am. Chem. Soc.*, 2004, **126**, 13176-13177.
22. T. Yamamoto, Y. Umemura, O. Sato and Y. Einaga, *J. Am. Chem. Soc.*, 2005, **127**, 16065-16073.
23. F. Herren, P. Fischer, A. Ludi and W. Halg, *Inorg. Chem.*, 1980, **19**, 956-959.
24. A. Ludi, H.-U. Gcdel and M. Ruegg, *Inorg. Chem.*, 1970, **9**, 2224-2227.
25. S. Vaucher, M. Li and S. Mann, *Angew. Chem. Int. Ed.*, 2000, **39**, 1793-1796.
26. M. B. Robin, *Inorg. Chem.*, 1962, **1**, 337-342.
27. Y. Y. Song, W. Z. Jia, Y. Li, X. H. Xia, Q. J. Wang, J. W. Zhao and Y. D. Yan, *Adv. Funct. Mater.*, 2007, **17**, 2808-2814.
28. Y. Yue, A. J. Binder, B. Guo, Z. Zhang, Z. A. Qiao, C. Tian and S. Dai, *Angew. Chem. Int. Ed.*, 2014, **53**, 3134-3137.
29. Y. Xian, Y. Hu, F. Liu, Y. Xian, L. Feng and L. Jin, *Biosens. Bioelectron.*, 2007, **22**, 2827-2833.
30. N. Zhu, S. Han, S. Gan, J. Ulstrup and Q. Chi, *Adv. Funct. Mater.*, 2013, **23**, 5297-5306.
31. S. Wu, Y. Liu, J. Wu and H. Ju, *Electrochem. Commun.*, 2008, **10**, 397-401.
32. Q. Wang and D. O'Hare, *Chem. Rev.*, 2012, **112**, 4124-4155.
33. T. Kwon, G. A. Tsigdinos, T. J. Pinnavaia, *J. Am. Chem. Soc.*, 1988, **110**, 3653-3654.
34. R. Ma and T. Sasaki, *Adv. Mater.*, 2010, **22**, 5082-5104.
35. S. He, C. Li, H. Chen, D. Su, B. Zhang, X. Cao, B. Wang, M. Wei, D. G. Evans and X. Duan, *Chem. Mater.*, 2013, **25**, 1040-1046.
36. R. Liang, R. Tian, W. Shi, Z. Liu, D. Yan, M. Wei, D. G. Evans and X. Duan, *Chem. Commun.*, 2013, **49**, 969-971.
37. M. Shao, F. Ning, J. Zhao, M. Wei, D. G. Evans and X. Duan, *Adv. Funct. Mater.*, 2013, **23**, 3513-3518.
38. L. Liang, J. Zhang, Y. Zhou, J. Xie, X. Zhang, M. Guan, B. Pan and Y. Xie, *Sci. Rep.*, 2013, **3**, 1936-1943.
39. L. Li, R. Ma, Y. Ebina, K. Fukuda, K. Takada and T. Sasaki, *J. Am. Chem. Soc.*, 2007, **129**, 8000-8007.
40. E. Coronado, C. Martí-Gastaldo, E. Navarro-Moratalla, A. Ribera, S. J. Blundell and P. J. Baker, *Nat. Chem.*, 2010, **2**, 1031-1036.
41. X. Liu, R. Ma, Y. Bando and T. Sasaki, *Adv. Mater.*, 2012, **24**, 2148-2153.
42. R. Liang, D. Yan, R. Tian, X. Yu, W. Shi, C. Li, M. Wei, D. G. Evans and X. Duan, *Chem. Mater.*, 2014, **26**, 2595-2600.
43. D. Yan, J. Lu, M. Wei, S. Qin, L. Chen, S. Zhang, D. G. Evans and X. Duan, *Adv. Funct. Mater.*, 2011, **21**, 2497-2505.
44. J. Zhao, X. Kong, W. Shi, M. Shao, J. Han, M. Wei, D. G. Evans and X. Duan, *J. Mater. Chem.*, 2011, **21**, 13926.
45. J.-D. Qiu, H.-Z. Peng, R.-P. Liang, J. Li and X.-H. Xia, *Langmuir*, 2007, **23**, 2133-2137.
46. R. E. Wilde, S. N. Ghosh and B. J. Marshall, *Inorg. Chem.*, 1970, **9**, 2512-2516.
47. K.-K. Chiang and J.-J. Wu, *ACS Appl. Mater. Interfaces*, 2013, **5**, 6502-6507.
48. K. Lee, A. Y. Kim, J. H. Park, H.-G. Jung, W. Choi, H. Y. Lee and J. K. Lee, *Appl. Surf. Sci.*, 2014, **313**, 864-869.
49. J. Zhang, J.-P. Tu, D. Zhang, Y.-Q. Qiao, X.-Q. Xia, X.-L. Wang and C.-D. Gu, *J. Mater. Chem.*, 2011, **21**, 17316-17324.
50. G. Cai, X. Wang, M. Cui, P. Darmawan, J. Wang, A. L.-S. Eh and P. S. Lee, *Nano Energy*, 2015, **12**, 258-267.
51. J. Z. Ou, S. Balendhran, M. R. Field, D. G. McCulloch, A. S. Zoolfakar, R. A. Rani, S. Zhuiykov, A. P. O'Mullane and K. Kalantar-zadeh, *Nanoscale*, 2012, **4**, 5980-5988.
52. D. D. Yao, R. A. Rani, A. P. O'Mullane, K. Kalantar-zadeh and J. Z. Ou, *J. Phys. Chem. C*, 2014, **118**, 476-481.
53. C. Yan, W. Kang, J. Wang, M. Cui, X. Wang, C. Y. Foo, K. J. Chee and P. S. Lee, *ACS Nano*, 2014, **8**, 316-322.
54. G.-F. Cai, J.-P. Tu, C.-D. Gu, J.-H. Zhang, J. Chen, D. Zhou, S.-J. Shi and X.-L. Wang, *J. Mater. Chem. A*, 2013, **1**, 4286-4292.
55. X. W. Sun and J. X. Wang, *Nano Lett.*, 2008, **8**, 1884-1889.